The effect of particle size on flow in a continuous oscillatory baffled reactor using CFD

Guillermo Jimeno[a], Yeaw Chu Lee[b] and Xiong-Wei Ni[a]*

[a] EPSRC, Centre for Continuous Manufacturing and Crystallisation (CMAC), Centre for Oscillatory Baffled Reactor Applications (COBRA), School of Engineering and Physical Science, Chemical Engineering, Heriot Watt University, Edinburgh. EH14 4AS, UK

[b] School of Engineering and Physical Science, Mechanical Engineering, Heriot Watt University, Edinburgh. EH14 4AS, UK

*Corresponding author; email: x.ni@hw.ac.uk; Tel: 00441314513781

ABSTRACT

Experimental and numerical studies of flow characteristics in continuous oscillatory baffled reactors (COBR) have mainly been based on single liquid phase in the past decades. This work, for the first time, investigates the effects of particle size on axial dispersion and evaluates the residence time and velocity experienced by solid particles in a COBR, along with their impact on solid suspension. Computational fluid dynamics (CFD) methodology was employed for this work by coupling a primary Eulerian liquid phase with a secondary discrete Lagrangian phase consisting of solid particles of given density and size. The data not only provide insights on how particles behave in a COBR, but also assist the design and development of COBR.

Keywords: *axial dispersion of solids; RTD of solids; oscillatory baffled reactor; computational fluid dynamics (CFD); Eulerian-Lagrangian.*

1. Introduction

Oscillatory Baffled Reactors (OBR) offer uniform mixing[1] and linear scale up[2], making them an attractive alternative to stirred tank reactors for research and industrial applications in reaction[3-7] and crystallization processes[8-16]. The characterization of flows in COBR has extensively been reported using single phase[17-29] in the past decades. Recent work by Ejim et al.[30] highlighted the differences and the knowledge gap on the design of COBRs for multi-phase flow processes using correlations obtained from single phase studies; this was further emphasised by Kacker et al.[31] who reported that not only the optimal operating conditions for minimal axial dispersion involving solids were different from that of single phase, but also longer times were spent by solids in a COBR, highlighting the need to properly address the effect of different solid particles on axial dispersion. Baptista et al.[32] analyzed the behavior of suspended solid particles of different sizes and densities in a baffled reactor; however, their system did not include oscillatory flow and their findings were inconclusive, as the interaction among particles was too significant for the effects of size and density to be evaluated.

From a modelling standpoint, Computational Fluid Dynamics (CFD) solvers have been developed and used to simulate hydrodynamic flow profiles in OBRs/COBRs for multiple purposes[33-39]. Again, all these studies were performed under a single liquid phase framework, including the work by Mazubert et al.[40], who made use of discrete particle tracking of a secondary phase to measure concentration profiles and analyze the performance of different geometric designs; however, their secondary phase consisted of massless particles that essentially followed the velocity field of the continuous Eulerian phase.

The present CFD work involves two phases and aims to investigate the effect of particle size on axial dispersion in COBRs, while evaluating the residence times and velocities experienced by these solid particles and their impact on solids suspension. To the authors' best knowledge, this is the first study of its kind in the area of COBR where a continuous Eulerian phase is coupled with a discrete Lagrangian (solid) phase.

2. Problem definition

The dimensionless numbers that govern the conditions of the flow in a COBR are the net flow Reynolds numbers ($Re_n = u_{net\text{-}inlet}\rho D/\mu$), the oscillatory Reynolds number ($Re_o =$

$\omega x_o \rho D/\mu$), the Strouhal number (St = $D/4\pi x_o$), the ratio of the area of the orifice over the area of the tube, known as the restriction ratio ($\alpha = D_b^2 / D^2$), and the velocity ratio ($\Psi = Re_o/Re_n$); where ρ and μ are, respectively, the fluid density (kg m^{-3}) and dynamic viscosity (kg m^{-1} s^{-1}), D is the diameter of the tube (m), D_b the diameter of the baffle hole (m), $\omega=2\pi f$ the oscillation angular frequency (rad s^{-1}), x_o the oscillation center-to-peak amplitude (m), f the oscillation frequency (Hz) and $u_{net\text{-}inlet}$ is the net inlet velocity (m s^{-1}).

It should be noted that $u_{net\text{-}inlet}$ was carefully labeled to avoid any confusion with u_{net} as $u_{net} \neq u_{net\text{-}inlet}$. The net volumetric flow rate (Q) is constant and the net velocity at the inlet ($u_{net\text{-}inlet}$) is thus calculated as Q/A. However, while both Q and $u_{net\text{-}inlet}$ are constants, the net velocity changes along the length of the reactor due to its smooth-edged baffles, as shown in Figure 1, e.g. the volume of fluid flowing through a baffled constriction is 25% less than that of a cylinder of a diameter D, indicating $V \neq L \cdot A$ in this case; subsequently, the velocity through orifices ($u_{net\text{-}baffle}$) is defined as Q/A_b and the *mean* net velocity (u_{net}) of the system is within the range $Q/A \leq u_{net} \leq Q/A_b$. If the volume of the device is known, u_{net} is calculated as QL/V.

The target device of this study is a NiTech DN15 COBR reactor, as shown in Figure 1, the geometric dimensions of the DN15 and all design details were provided by the manufacturer, Alconbury Weston Ltd (http://www.a-w-l.co.uk/); the total length of the reactor is 752 mm, containing 32 baffle-cells. The operating oscillatory conditions were chosen partially based on the characteristics of the simulated particles, the simulated domain and literature work. Kacker et al. [31] used a net flow rate of 100 ml min^{-1} and identified an oscillatory amplitude of 2 mm and frequency of 2 Hz as optimal conditions for solid suspension and near plug flow behaviour of melamine crystals (mean particle size = 100 µm). Hence, Q = 100 ml min^{-1} and f = 2 Hz were selected for this study.

Extensive literature has reported a proportional relationship between oscillatory amplitude and axial dispersion[19-21,27,31,41]. However, while minimal dispersion and near plug flow behaviour are desirable, Oliva et al. [42] stated that the minimal energy required to ensure solid suspension should be considered. For this reason and considering paracetamol particles of up to 150 µm in diameter were simulated in this work, a moderate oscillatory amplitude of x_o = D_b (7 mm) was selected based on the work by González-Juárez et al. [39]. It should be noted that while the chosen 7 mm amplitude is within the reported range for RTD studies in DN15

[31,42], it is lower than that used in crystallization processes in COBRs where it commonly ranged from 12 to 30 mm [15,16,43-45] [references].

Due to the nature of oscillatory flow in COBRs, forward and backward mixing are generated during oscillation, resulting in particles flowing in and out of a control domain. It is thus crucial to select the injection point for solid phase as well as the measuring points to ensure that open boundary effects on particles, due to the inlet and outlet, are minimized. In terms of the injection point, it was set at the baffle-cell number 15, i.e. 352.5 mm from the inlet, which ensured that less than 0.1% of the injected particles left the system through the inlet for all the simulated conditions, see Table 1. Figure 2 displays a sketch of the injection point and measuring cells in the control zone of this work. The position and velocity of every injected particle are extracted and stored at every simulated time-step; this information is post-processed to calculate concentration profiles at any given measuring point. Effectively, measuring cells act as laboratory concentration probes, monitoring the number of particles present within their baffle-cells. For example, a measuring point (M) accounts for the particles contained within a distance of $L_b M \pm (L_b/2)$, where M ranges from 0 to 32. Collectively, concentration of particles (#particles m^{-3}) is monitored over the whole domain, i.e. the total number of monitored particles coincides with the total number of particles present in the system at all times. The optimal measuring points for the conditions tested in this study were identified as baffle-cell numbers from 17 to 27 (Figure 2), ensuring that over 99.9% of the injected particles pass through these measuring points as they move downstream; further discussion on the selection of measuring points is in section 5.2.

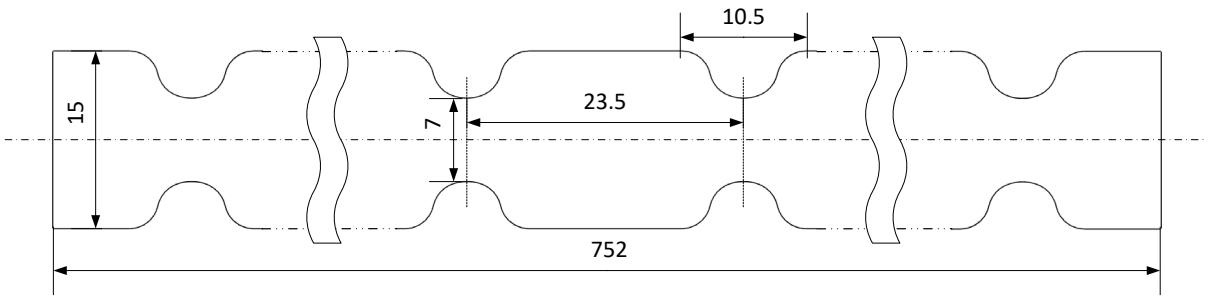

Figure 1. *Dimensions of the NiTech DN15 straight section used in CFD simulations; all quotes are in mm*

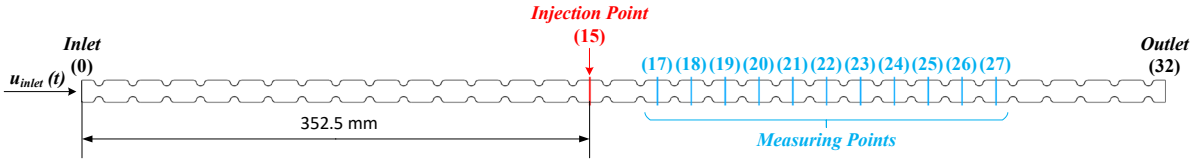

Figure 2. *Definition of the injection and measuring points across the NiTech DN15*

Table 1. *List of all simulated conditions*

Run #	Q (ml min^{-1})	f (Hz)	x_o (mm)	Re_n	Re_o	Material injected	$D_{particle}$ (µm)
1	100	2	5	141	938	Tracer (massless)	–
2	100	2	7	141	1313	Tracer (massless)	–
3	100	2	7	141	1313	Paracetamol	50
4	100	2	7	141	1313	Paracetamol	100
5	100	2	7	141	1313	Paracetamol	150

3. Determination of axial dispersion

In a tubular reactor, mixing is commonly quantified by axial dispersion coefficient (D_a), which describes the degree of spreading (in the axial direction) of a tracer injected upstream as a pulse (ideally). Analogous to the molecular diffusion model, Levenspiel and Smith [46] proposed the following equation to evaluate the axial dispersion coefficient:

$$\frac{\partial C}{\partial t} = D_a \frac{\partial^2 C}{\partial x^2} - U \frac{\partial C}{\partial x} \tag{1}$$

where C is the tracer concentration as a function of time (t) and position (x) and U is the mean net flow velocity of the system ($U = QL/V$). Equation (1) was originally derived for a single phase flow and could also be used for two phase (solid – liquid) cases. When the concentration of a liquid tracer is defined as $C_L = m_L/V_L$ and the concentration of solids as $C_S = m_S/(V_L + V_S)$, eq. (1) becomes independent of the volume of the secondary solid phase ($V_L + V_S \approx V_L$) when $V_S << V_L$, which is the case in the present study. This is also consistent with literature, e.g. the work of Ejim et al.[30] and Kacker et al.[31]. If a perfect input pulse injection is assumed, typical boundary conditions for eq. (1) are:

$$C(x,0) = \frac{n}{A}\delta(x) \tag{2.1}$$

$$\lim_{x\to\pm\infty} C(x,\mathrm{t}) = 0 \tag{2.2}$$

where n is the volume of tracer/secondary phase injected, A the cross-sectional area of the device and $\delta(x)$ a Dirac delta function. Thus, the analytical solution to equations (1) and (2) at fixed values of D_a and U is given by

$$C(x,t) = \frac{1}{\sqrt{4\pi D_a t}}\exp\left(-\frac{(x-Ut)^2}{4D_a t}\right) \tag{3}$$

Under the assumption of a perfect pulse injection, the plug flow with axial dispersion model can be re-derived and solved based on an inverse Peclet number ($Pe = UL/D_a$) as:

$$\sigma_\theta{}^2 = \frac{\sigma^2}{\overline{t}^2} = 2\frac{1}{Pe} + 8\left(\frac{1}{Pe}\right)^2 \tag{4}$$

where $\sigma\theta^2$ is the dimensionless variance, σ^2 the variance and $(\overline{t})$ the mean residence time of the tracer concentration as:

$$\sigma^2 = \frac{\int_0^\infty (t-\overline{t})^2 C(t)\,dt}{\int_0^\infty C(t)\,dt} = \frac{\sum_{i=1}^{N}(t_i-\overline{t})^2 C(t_i)\Delta t_i}{\sum_{i=1}^{N} C(t_i)\Delta t_i} \tag{5}$$

$$\overline{t} = \frac{\int_0^\infty tC(t)\,dt}{\int_0^\infty C(t)\,dt} = \frac{\sum_{i=1}^{N} tC(t_i)\Delta t_i}{\sum_{i=1}^{N} C(t_i)\Delta t_i} \tag{6}$$

where N is the total number of measured concentration data. Eq. (4) is used to evaluate axial dispersion coefficient under the perfect pulse method (PPM).

A perfect input pulse is virtually unachievable. Hence, an imperfect pulse method (IPM) was proposed [47] where the concentration profile of the tracer/secondary phase is measured at two downstream points of the tracer injection, i.e. $C_1(t)$ and $C_2(t)$; thus the form of the impulse becomes irrelevant. This method was firstly implemented in OBRs by Mackley and Ni [1], who adopted the solution of Göeble et al. [48] and used a normalized concentration $E(t)$ for better comparison among results:

$$E(t) = \frac{C(t)}{\int_0^\infty C(t)\,dt} = \frac{C(t_i)}{\sum_{i=1}^{N} C(t_i)\,\Delta t_i} \tag{7}$$

Mackley and Ni [1] suggested that the normalized concentration measured at an upstream point (1) during a short time interval (Δt) can be regarded as a perfect pulse injection made at such point, with an injected volume $E(t_1)\Delta t$ at time $t = t_1$. Taking the limit $\Delta t \rightarrow 0$ and integrating over all possible injection times (t_1), the normalized concentration at point (2) can be estimated by the convolution integral equation below:

$$E_2'(t) = \int_0^t E_1(t_1)\,TR(t-t_1)\,dt_1 = \sum_{i=1}^{N} E_1(t_{1,i})\,TR(t-t_{1,i})\,\Delta t_{1,i} \tag{8}$$

where $TR(t)$ is the transfer function for "open-open" boundary conditions. The formulation of the transfer function reported by Mackley and Ni was in disagreement with the one proposed by Westerterp et al. [49]. However, later work by Smith [50] proved that the formulation of Westerterp et al. was the most accurate, hence it is used in the current work as:

$$TR(t) = \frac{1}{\sqrt{4\pi D_a \frac{t^3}{L^2}}} \exp\left(-\frac{(L-Ut)^2}{4D_a t} \right) \tag{9}$$

where the distance from the injection point (L) is essentially the distance between measuring points (1) and (2). The normalized concentration predicted at point (2), $E_2'(t)$, is compared with the measured normalized concentration at such point, $E_2(t)$, and the axial dispersion coefficient is fitted in order to satisfy the target function:

$$\Delta E = \sum_{i=1}^{N} \left\{ E_2(t_i) - E_2'(t_i) \right\}^2 \tag{10}$$

where N is the total number of normalized concentration data. The optimal axial dispersion coefficient is obtained when the target function (10) is minimized. While the value of the mean net flow velocity (U), as aforementioned, can be assumed as $U = u_{net}$, a better method is to calculate the time it takes for the tracer/secondary phase to travel from measuring point (1) to (2) as:

$$U = \frac{L}{\int_0^\infty tE_2(t)\,dt - \int_0^\infty tE_1(t)\,dt} = \frac{L}{\sum_{i=1}^{N} tE_2(t)\Delta t - \sum_{i=1}^{N} tE_1(t)\Delta t} \tag{11}$$

The imperfect pulse method [20,24,26,41,51] [38] as well as the perfect pulse method [31,42] [39,40] have been used to quantify axial dispersion in COBRs. Consequently, both methods (PPM and IPM) are used in this work, enabling comparison and assessment of the impact of length (from injection to measuring point) on their accuracy. For better comparison, most of the RTD curves reported in this work are presented in their normalized form as $E(\theta)$ vs θ, where $E(\theta) = \overline{t}\,E(t)$ and $\theta = t/\overline{t}$.

4. Computational simulation set-up

All numerical simulations were performed using ANSYS® Fluent 16.0 CFD package, which discretizes a computational domain using finite volume methodology in order to solve the flow field of a continuous phase. Additionally, Fluent allows for Lagrangian particle tracking by implementing a so-called Discrete Phase Model (DPM) as an add-on to an existing Eulerian phase, this capability was utilized to model massless (tracer) and solid particles.

4.1. Numerical model for Eulerian phase

The fluid selected for this study was water (ρ = 998.2 kg m^{-3}, μ = 1.003·10^{-3} kg m^{-1} s^{-1}); time-dependent incompressible three-dimensional Navier-Stokes equations were solved as:

$$\nabla \cdot \vec{u} = 0 \tag{12}$$

$$\rho\left(\frac{\partial \vec{u}}{\partial t} + \vec{u} \cdot \nabla \vec{u}\right) = \rho \vec{g} - \nabla p + \mu \nabla^2 \vec{u} \tag{13}$$

All simulations were performed utilizing a pressure-based segregated solver along with the SIMPLE pressure-velocity coupling algorithm. Spatial discretization of the momentum equation was performed using a *second order upwind* scheme; pressure at faces of the grid was interpolated using a *second order* scheme and time was discretized using a *first order implicit* scheme. The time-step was set to 2 ms, ensuring a good number of time-steps per oscillatory cycle of 250, which is higher than the norm reported in literature [39,40]. The average and maximum values of the Courant–Friedrichs–Lewy (CFL) coefficient were consistently kept below 2 and 20 respectively.

Because of the low net flow and oscillatory Reynolds numbers of the conditions simulated, a laminar solver was selected. This is also in agreement with existing literature [35,38-40,52-55]. The impact of inlet boundary conditions on the main flow was minimized by imposing a fully developed parabolic profile: $u_{inlet}(r,t) = 2 \cdot u(t) \cdot \left(1 - \frac{r^2}{R^2}\right)$, where $u(t) = u_{net-inlet} + \omega x_o \sin(\omega t)$. A constant gauge pressure of 0 Pa was set for the outlet boundary; operating conditions were set at 300 K and 101325 Pa.

4.1.1. Mesh sensitivity test

A 5-baffle-cell tube geometry was employed for the performance of a mesh sensitivity study, as illustrated in Figure 3. This analysis was previously undertaken during a power density study in COBRs [56] [UPDATE], under its most adverse conditions (Q = 50ml min^{-1}, f = 8Hz, x_o = 14mm). The time-step was set to 0.5 ms for an oscillatory cycle consisting of 250 time-steps. Considering global mesh refinement, five meshes of different resolutions were compared and each simulation was run for 24 oscillatory cycles. The variables compared

between meshes were pressure drop vs time profiles ($\Delta p(t) = p_1(t) - p_2(t)$) and velocity magnitude vs time profiles extracted at lines 1 & 2 and planes 1 & 2 as shown in Figure 3. These profiles were cycle-averaged and the resultant profiles (of the duration of an oscillatory cycle) were compared using the coefficient of determination (R^2):

$$R^2 = 1 - \frac{SS_{res}}{SS_{tot}} = 1 - \frac{\sum_{i=1}^{n} \left(\phi_{j,i} - \phi_{1,i} \right)^2}{\sum_{i=1}^{n} \left(\phi_{1,i} - \overline{\phi_{1,i}} \right)^2} \tag{14}$$

where SS_{res} is the sum of squares of residuals between the target profile (that from mesh #1) and the profile under evaluation (from mesh #j) and SS_{tot} is the total sum of squares of the target profile. Subscripts i and n represent a single data point and the total number of data points of a certain profile respectively, while j is the index of a certain mesh and ϕ the property under evaluation.

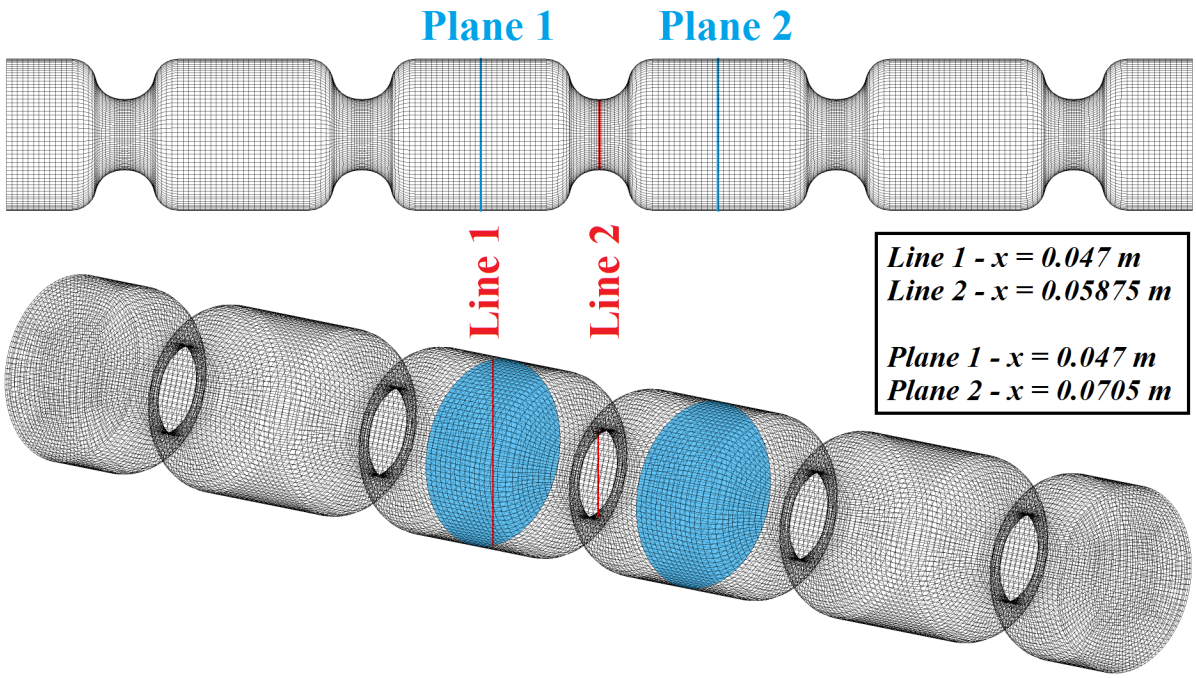

Figure 3. *Five-baffle-cells geometry, lines and planes where variables were monitored during mesh independency test*

The profiles extracted from each mesh were compared to those from mesh #1. The results of this mesh sensitivity analysis are summarized in Table 2; Mesh #2 (in bold) was selected on the balance of accuracy and efficiency, and its density is above the norm reported in literature[36,38,52,54,57-59]. All meshes were created on ANSYS ICEM containing only hexahedral elements and were O-grid structured.

Table 2. *Mesh sensitivity analysis results (Q = 50ml min-1, f = 8Hz, x_o = 14mm)*

			Velocity Magnitude at			
Mesh	# Nodes*	Δp**	Line 1	Line 2	Plane 1	Plane 2
1	236 k	–	–	–	–	–
2	**117 k**	**0.978**	**0.990**	**0.997**	**0.995**	**1.000**
3	64 k	0.940	0.984	0.996	0.984	0.999
4	31 k	0.922	0.984	0.996	0.980	0.999
5	7 k	0.670	0.911	0.989	0.825	0.997

* *Number of nodes per baffle-cell.*
** *Pressure drop profile between planes 1 and 2:* $\Delta p(t) = p_1(t) - p_2(t)$.

4.2. Numerical model for Lagrangian phase

The discrete solid phase was mono-sized spherical paracetamol (ρ = 1263 kg m^{-3}) particles of diameter (D_p) 50, 100 and 150 μm, while liquid phase information was obtained from discrete massless particles that act as a perfect tracer as they move according to the flow field of the continuous liquid phase. The trajectory of each discrete particle is predicted by integrating the force balance on the particle as:

$$m_p \frac{d\vec{u}_p}{dt} = \vec{F}_D + m_p \vec{g}\left(\frac{\rho_p - \rho}{\rho_p}\right) + \vec{F} \tag{15}$$

where m_p, $\vec{u}_p$ and ρ_p are, respectively, the mass, velocity and density of the particle. The second term in the right-hand side of eq. (15) accounts for the force due to the weight of the particle and the buoyancy effect, the first term $\vec{F}_D$ is the drag force defined as:

$$\vec{F}_D = \frac{1}{2}\rho C_D A_p \left|\vec{u} - \vec{u}_p\right|\left(\vec{u} - \vec{u}_p\right) \tag{16}$$

where A_p is the cross-sectional area of the particle and C_D is the drag force coefficient, calculated as the spherical drag law proposed by Morsi and Alexander [60]. The third term $\left(\vec{F}\right)$ includes the so-called "virtual mass" $\left(\vec{F}_{VM}\right)$ and the pressure gradient force $\left(\vec{F}_{PG}\right)$, the former accounts for the force required to accelerate the fluid surrounding the particle and the latter is the resultant force from the pressure gradient along the fluid flow around the particle:

$$\vec{F}_{VM} = \frac{1}{2} m_p \frac{\rho}{\rho_p} \left(\frac{D\vec{u}}{Dt} - \frac{d\vec{u}_p}{dt} \right) \tag{17}$$

$$\vec{F}_{PG} = m_p \frac{\rho}{\rho_p} \frac{D\vec{u}}{Dt} \tag{18}$$

where $\frac{D}{Dt}$ is the material derivative. The position of each particle $\left(\vec{x}_p\right)$ is governed by

$$\frac{d\vec{x}_p}{dt} = \vec{u}_p \tag{19}$$

Equations (15) and (19) are integrated using a trapezoidal discretization scheme with the same time-step as the Eulerian phase (2 ms). All particles were modelled as perfect spheres and were released at a cross-sectional plane at the middle of a selected baffle-cell; this is the so-called "surface injection". In order to cope with the potential computational limitation of modelling too many particles, Fluent tracks so-called "parcels". A parcel may contain multiple particles; its position is defined by a tracked representative particle and its diameter is that of a sphere whose volume is the ratio of the total parcel mass to particle density. However, in this work, in order to model and predict the behavior of individual particles, the mass of each parcel was set as that of a single particle, i.e. each parcel contained one particle and thus the concept of parcel and particle are interchangeable in this study. The number of particles released in the system was set to 4050; further analysis on the sensitivity of the number of tracked particles on results will be discussed on section 5.1. No particle – particle interaction or particle diffusion in the liquid phase were included in the model.

5. Results

5.1. Effect on number of simulated particles

Discrete particles were injected into a cross-sectional plane in the middle of a baffle-cell containing 4050 computational cells; the "surface" injection type releases one particle per computational cell, thus 4050 particles were injected. This number is significantly larger than what is reported in literature, e.g. Mazubert et al. [40] examined the effect of the number of injected particles (2484 and 4968) on the simulated results and found that the difference between the two was negligible. Taking a conservative approach, particle numbers of 4050 and 8100 were examined and compared in this work; for the latter, the "surface" injection was simultaneously performed at two cross-sectional planes in the middle of the 15th baffle-cell, with a distance of 0.75 mm apart. This analysis was performed for massless particles under the operating conditions of run #2 (see Table 1). Figure 4 (left) displays the profiles of $E(\theta)$ vs θ measured at the baffle-cell (27) for both types of injection; the degree of agreement between profiles is very good. Additionally, the axial dispersion coefficients calculated using the PPM, eq. (4), and the IPM, equations (8) – (11), at different lengths of the reactor for both numbers of injected particles are presented in Figure 4 (right). Again, the agreement between results is remarkable. Results obtained with the IPM were calculated using the baffle-cell (17) as C_1 and baffle-cells (19) – (27) as C_2. On balance of accuracy and computing time, it was determined that a "surface" injection of 4050 particles is sufficient for reproducing the flow patterns in the COBR.

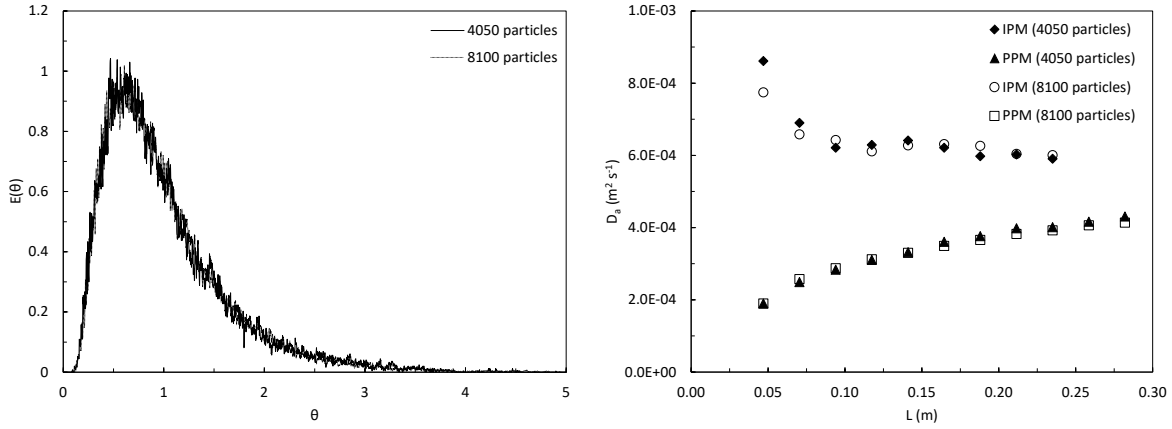

Figure 4. *E(θ) vs θ profiles (left) and Da vs L (right) for two numbers of injected discrete phase particles at operating conditions of run #2.*

5.2. Measuring points

While CFD simulated RTD curves can be monitored at any length of the reactor, the effect of "open-open" boundary conditions must be taken into account. Due to the oscillatory nature of the flow, particles would pass through a certain section of the domain multiple times, as the oscillatory velocities are considerably higher than the net flow velocity; for this reason, measuring points must cautiously be selected. If a measuring point is too close to an open boundary, particles would escape the system prematurely. In order to select appropriate measuring points, RTD curves were monitored and the areas under the curves $\left(C_o = \int_0^\infty C(t)\,dt = \sum_{i=1}^{N} C(t_i)\,\Delta t_i \right)$ calculated for all baffle-cells of the modeled device, C_o values were then plotted as a function of length (from the injection point) in Figure 5 (right); RTD curves measured at three different baffle-cells during run #2 are presented in Figure 5 (left).

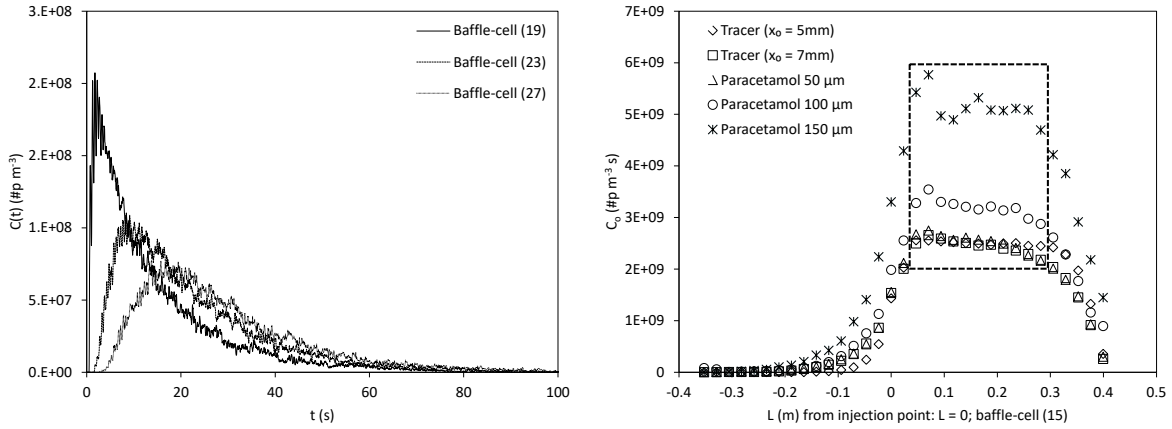

Figure 5. *RTD curves measured at different baffle-cells at operating conditions of run #2 (left) and RTD area under the curve (C_o) with length for all simulated conditions (right)*

A constant C_o value for each simulated run is a good guide for selecting measuring points, see the framed square in Figure 5 (right). Consequently, RTD data obtained from baffle-cells (17) to (27) (0.047 – 0.282 m from the injection point) was selected for analysis, while the remaining concentration profiles measured at baffle-cells (28) to (32) were discarded as the effect of the open boundary was too large for reliable $C(t)$ curves to be measured.

5.3. Perfect vs Imperfect pulse method

Figure 6 shows the axial dispersion coefficients obtained from both the PPM and IPM methods as a function of length for all runs (refer to Table 1). Results provided by IPM were calculated with baffle-cell (17) as C_1 and baffle-cells (19) – (27) as C_2. Results computed when baffle-cell (18) was set as C_2 were consistently higher than expected and have not been included; this shows a potential limitation of IPM, which may occur when both measuring points are too close to each other. Besides this phenomenon presented at $L < 2L_b$, IPM consistently provides stable results.

The results by PPM are undoubtedly dependent on the length at which RTD curves were measured; as a matter of fact, the length of the device over which this analysis has been performed is not sufficient for PPM to reach a completely asymptotic D_a value. On the other hand, IPM steadily reaches an asymptotic D_a value at a very early stage; such value was calculated as the average of results obtained when baffle-cells (20) to (27) were set as C_2. Although D_a values computed via IPM fluctuate around the asymptotic value, they are much more stable than their counterparts and are thus chosen as the final results in this study.

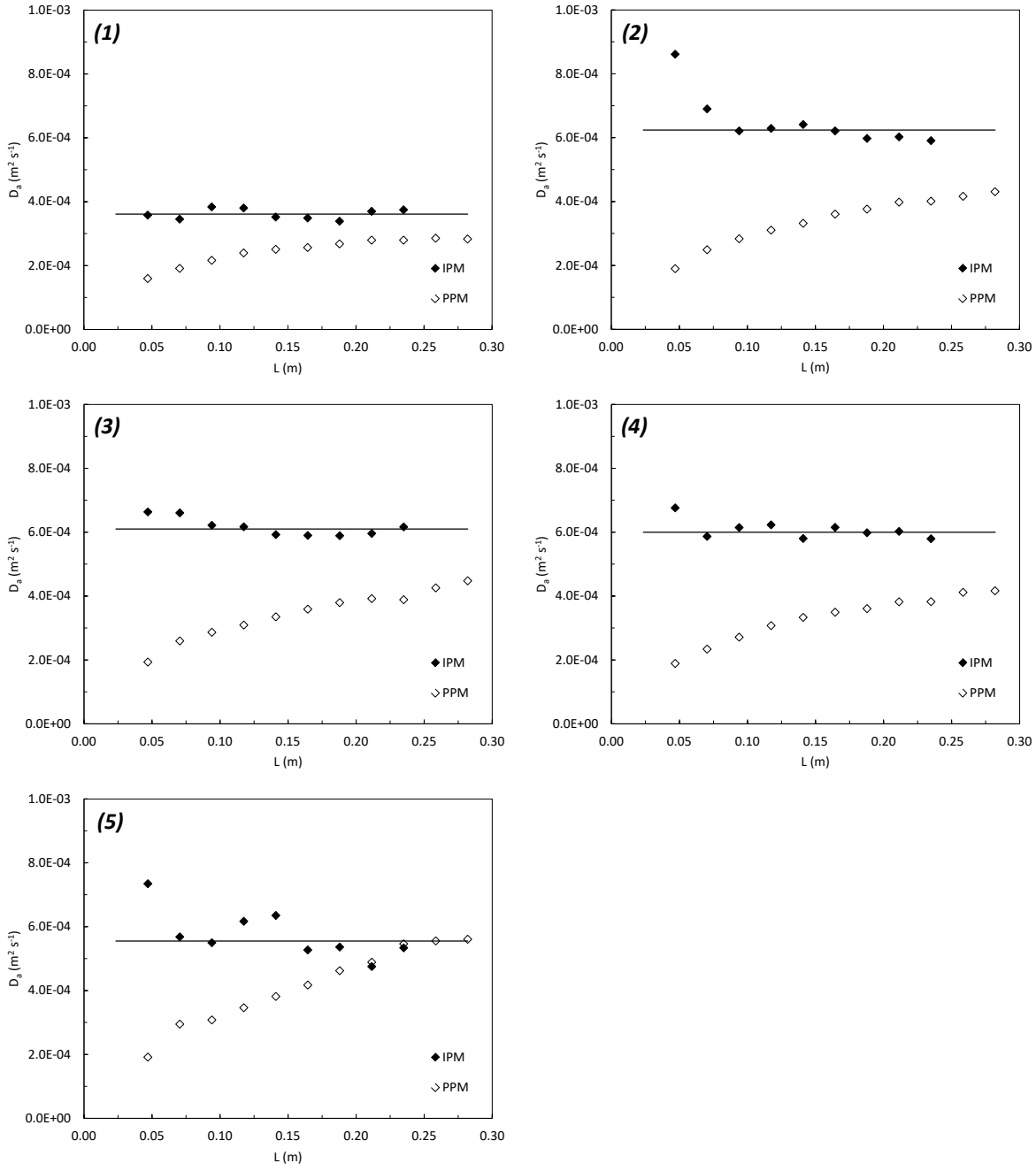

Figure 6. *D_a calculated from RTD curves measured at different lengths (from the injection point) using the imperfect (IPM) and the perfect pulse (PPM) methods for all runs simulated.*

During this analysis, it was observed how the residual errors from target function (10) were consistently higher when U was assumed to be equal to QL/V, as opposed to when it was calculated with eq. (11). Figure 7 shows the velocity values obtained during the fitting process of IPM, calculated via eq. (11) at different lengths of the reactor. In reality, U from eq. (11), presented in Figure 7, represents the mean net velocity particles experienced while

travelling from measuring point (1) to point (2). This velocity becomes more smoothed out as measuring point (2) is moved along the length of the device at a fixed measuring point (1), thereby increasing the length over which RTD curves are examined. Our preliminary results clearly indicate that while $U = QL/V$ is a fair estimation of liquid phase velocity, the velocity of a secondary solid phase is dependent on particle size, with velocity of small particles (50 μm diameter) close to that of the liquid phase and that of larger particles being significantly smaller. As a result, the assumption of $U = QL/V$ when applying the IPM was disregarded. Note that the discussion above refers to a secondary phase containing mono-size particles similar to those simulated in this work.

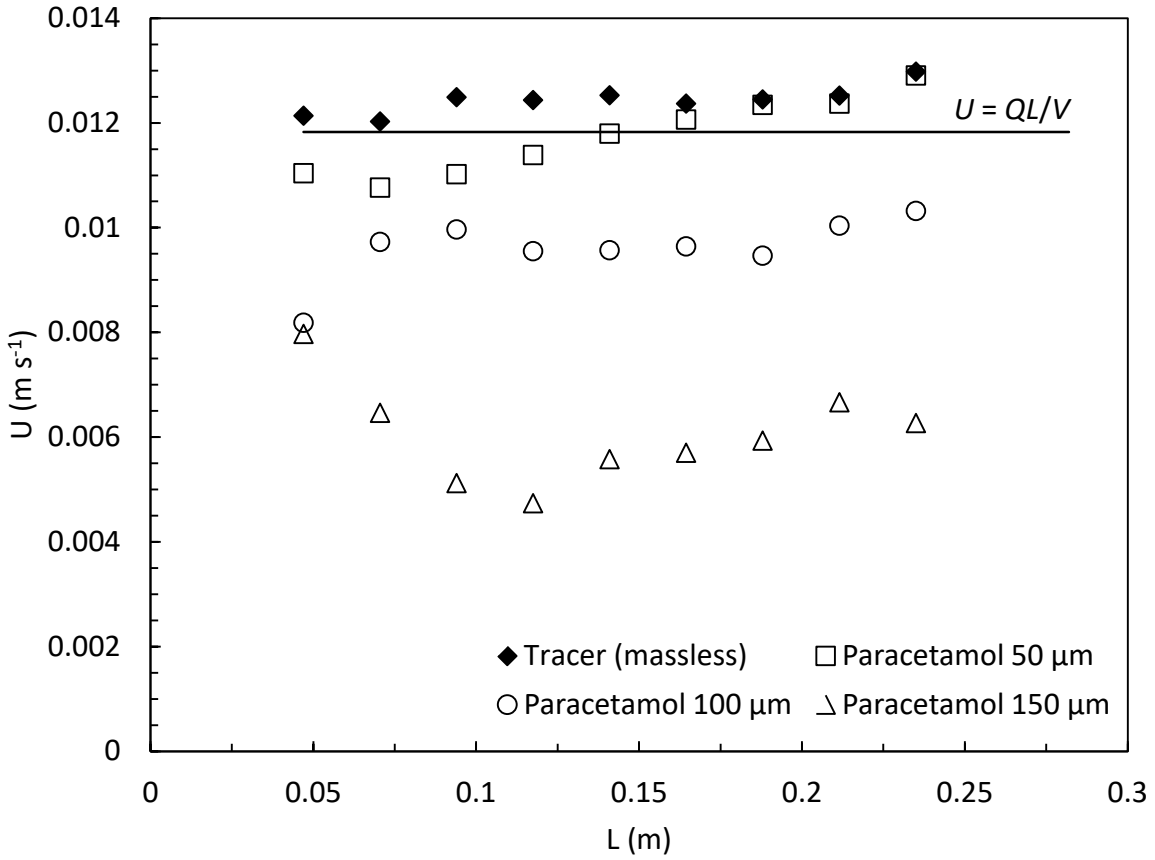

Figure 7. *Velocity calculated with eq. (11) with measuring point (1) fix at baffle-cell (17) and measuring point ranging from baffle-cell (19) to (27) (Q = 100ml/min, f = 2Hz, x_o = 7mm)*

5.4. Validation of simulated results

For the validation of our CFD methodology and the estimation of axial dispersion coefficients, results of Kacker et al.'s work [31] are compared with those obtained in this study.

Kacker et al. undertook their experimental investigation in a DN15 with very similar geometry to the one used in this work and analysed axial dispersion for a wide range of operating conditions using a homogenous tracer (methylene blue) and a heterogeneous phase (melamine). The results of their homogenous tracer are compared with that of our massless particles (asymptotic values from Figure 6) and plotted in Figure 8 (left). We see that the order of magnitude and the trend of D_a vs x_o bear great similarity to those of Kacker et al., thus validating our model.

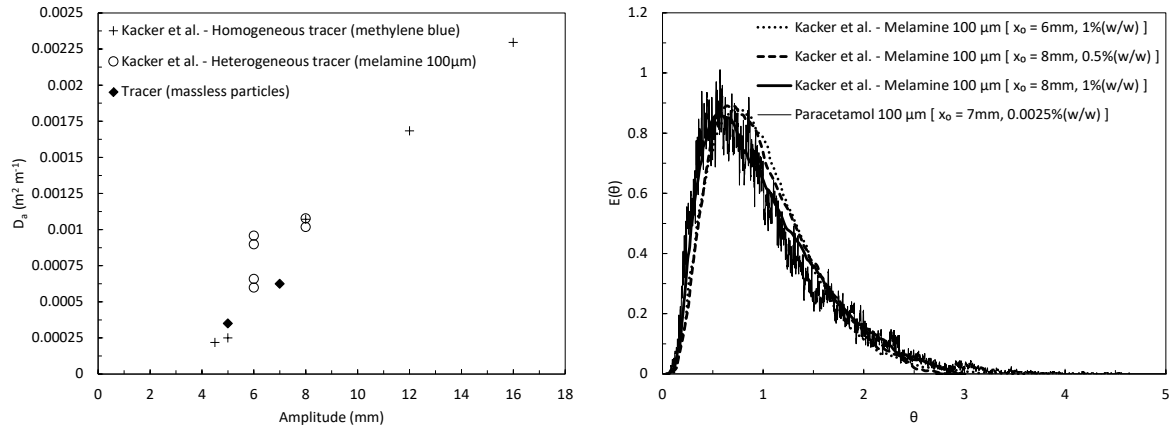

Figure 8. *Comparison with Kacker et al. results*

Figure 8 (left) also shows the axial dispersion coefficient obtained by Kacker et al. using melamine (ρ = 1575 kg m^{-3}) particles of 100µm mean particle size at different solid concentrations. While the effect of concentration on axial dispersion was not clear from the work of Kacker et al., their results pointed to an axial dispersion coefficient of around 0.0006 – 0.001 m^2 s^{-1} at oscillatory amplitude of 7mm. In the current study, a D_a of 0.0006 m^2 s^{-1} (asymptotic value from Figure 6) was obtained from run #4. By taking the density difference between the two studies into consideration and using the correlation by Ni et al. [25], D_a is multiplied by a density ratio ($\rho_{melamine}$ / $\rho_{paracetamol}$), giving a value of D_a = 0.000748 m^2 s^{-1}, which is within the range suggested by Kacker et al.

Additionally, despite the difference in density, RTD curves reported by Kacker et at. were digitally extracted using the online tool WebPlotDigitizer (https://automeris.io/WebPlotDigitizer/) for comparison. The $E(\theta)$ vs θ curves of their heterogeneous tracer were plotted along with that from run #4 of this work in Figure 8 (right).

The results they obtained from injection port 1 and measuring port 1 ($L \approx 0.72$ m) were chosen as the basis for comparison; the profile measured at baffle-cell (27) of our device ($L = 0.282$ m) shown in Figure 8 (right) has a remarkable similarity both in magnitude and shape, hence validating the simulated results of this work.

5.5. Effect of size of particle on axial dispersion and residence time

The effect of particle size on axial dispersion is graphically presented in Figure 9 (left), displaying profiles of $E(\theta)$ vs θ of the baffle-cell (27) for all runs performed (see Table 1). While the impact of particle size on axial dispersion of the secondary phase is qualitatively minimal (Figure 9 left), the asymptotic D_a values from Figure (6) decrease with the increase of particle size (Table 3). The mean residence time required for particles to reach baffle-cell (27) from the injection cell (15) becomes longer, displaying a noticeable shift in the profiles of $E(\theta)$ vs t (Figure 9 right). We see that the residence time for particles of 50 μm diameter barely changes in comparison to that of the liquid phase (represented by massless particles), whereas particles of 100 or 150 μm diameters suffer an increment in residence time of up to 139% (Table 3).

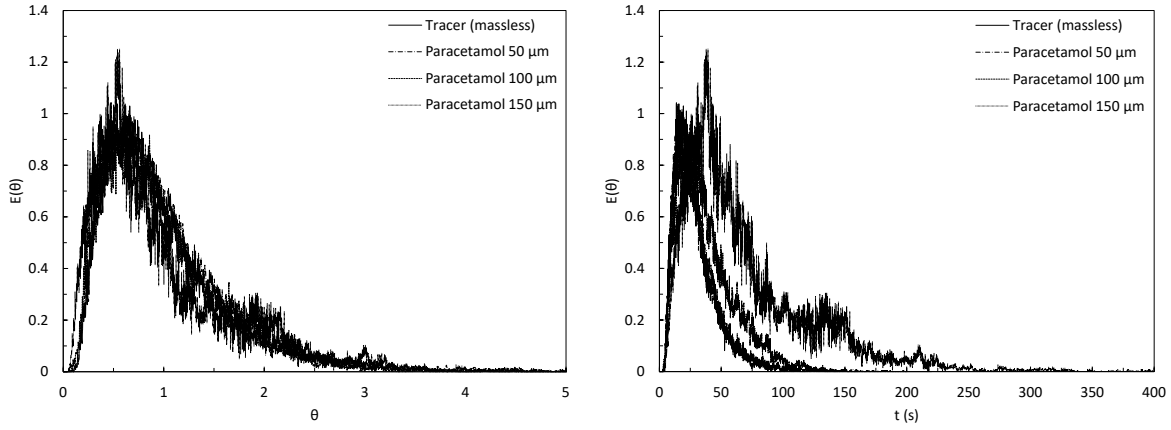

Figure 9. *E(θ) vs θ (left) and E(θ) vs t (right) profiles for different particle sizes (Q = 100ml/min, f = 2Hz, x_o = 7mm)*

Table 3. *Da and $\bar{t}$ values for different particle sizes (Q = 100ml/min, f = 2Hz, x_o = 7mm)*

D_a (m^2 s^{-1})	ΔD_a (%)††	$\bar{t}$ (s)**	$\Delta \bar{t}$ (%)††

Tracer (massless)	6.24E-04	–	29.3	–
Paracetamol 50 µm	6.10E-04	-2.2	29.6	0.9
Paracetamol 100 µm	6.00E-04	-3.9	38.1	29.9
Paracetamol 150 µm	5.55E-04	-11.1	70.1	138.9

[**] *Mean residence time at baffle-cell (27), where L (from injection point) = 0.282 m*
[††] *With respect to the values provided by the liquid phase (massless tracer)*

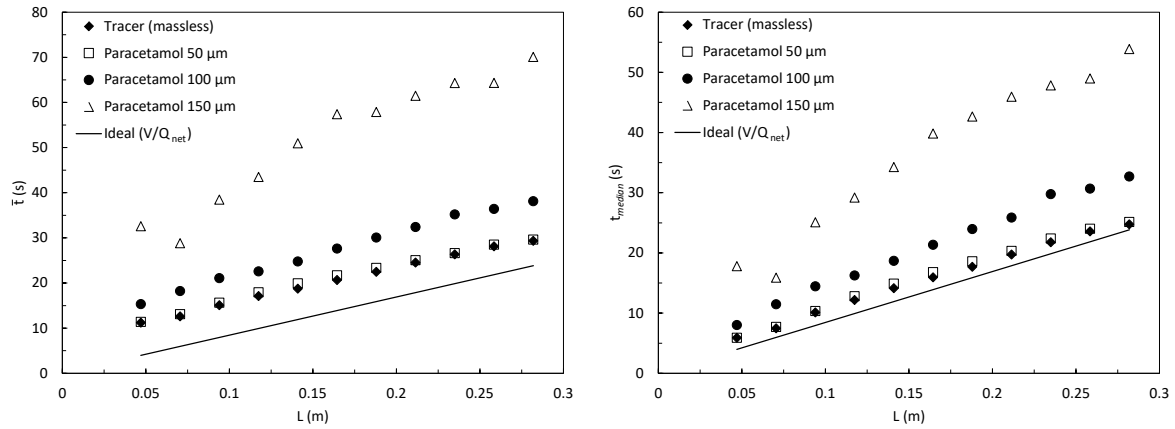

Figure 10. *Mean residence time as a function of length (from the injection point) for different particle sizes (Q = 100ml/min, f = 2Hz, x_o = 7mm)*

Figure 10 (left) shows the mean residence time spent by particles from baffle-cell (15) to (27) calculated via eq. (5), with $\bar{t} = V/Q_{net}$ as the basis for comparison. Due to the deviations of the RTD curves from Gaussian function (Figure 5 left), the mean residence time $\bar{t}$ is significantly smaller than its median residence times (t_{median}), Figure 10 (right) plots t_{median} as the function of length for the purpose of completion. We see that both mean and median residence times increase with particle size. This is due to decay in oscillatory axial velocity with the presence of particles, leading to smaller axial dispersion and longer residence times. These findings are consistent with the work of Ejim et al. and Kacker et al.[30,31] and should be considered when designing COBRs for crystallization processes where particles' residence time is a key factor affecting crystal growth.

It is also seen from Figure 10 that the slopes of increasing residence times for liquid phase and for solid phase (paracetamol of 50 µm diameter) are the same, indicating that both move axially at a constant mean net velocity. The slopes for particles of 100 and 150 µm diameter are moderately higher, denoting an increasing decay in their mean net velocities with length.

5.6. Effect of particle size on their velocity and suspension

In this work, the time-dependent velocity magnitude (u_m) and the velocity in the axial direction (u_x) were calculated as:

$$u_m(t) = \frac{\sum_{i=1}^{N(t)} u_{m,i}(t)}{N(t)} \tag{20.1}$$

$$u_x(t) = \frac{\sum_{i=1}^{N(t)} u_{x,i}(t)}{N(t)} \tag{20.2}$$

where the index i represents a specific particle. Because the total number of particles is a function of time, results for each simulated run are only reported till all particles have reached and left the baffle-cell (27), i.e. $t = \overline{t}_{baffle-cell-27}$ (Table 3), ensuring that no effects from the open boundary outlet are present. Figure 11 displays axial velocity profiles of particles of different sizes over a certain time frame, along with the inlet velocity profile as a basis of reference. Losses in oscillatory amplitude of 10, 21 and 45% for particles of 50, 100 and 150 μm respectively are clearly seen as particle size increases.

Figure 12 plots u_x with time for particles of different sizes. The liquid phase and small particles (50 μm) show a nearly constant trend of their oscillatory axial velocity peaks with time, while a decreasing trend in the magnitudes of oscillatory axial peaks is evident for paracetamol solids of 100 μm (left) and 150 μm (right) diameter.

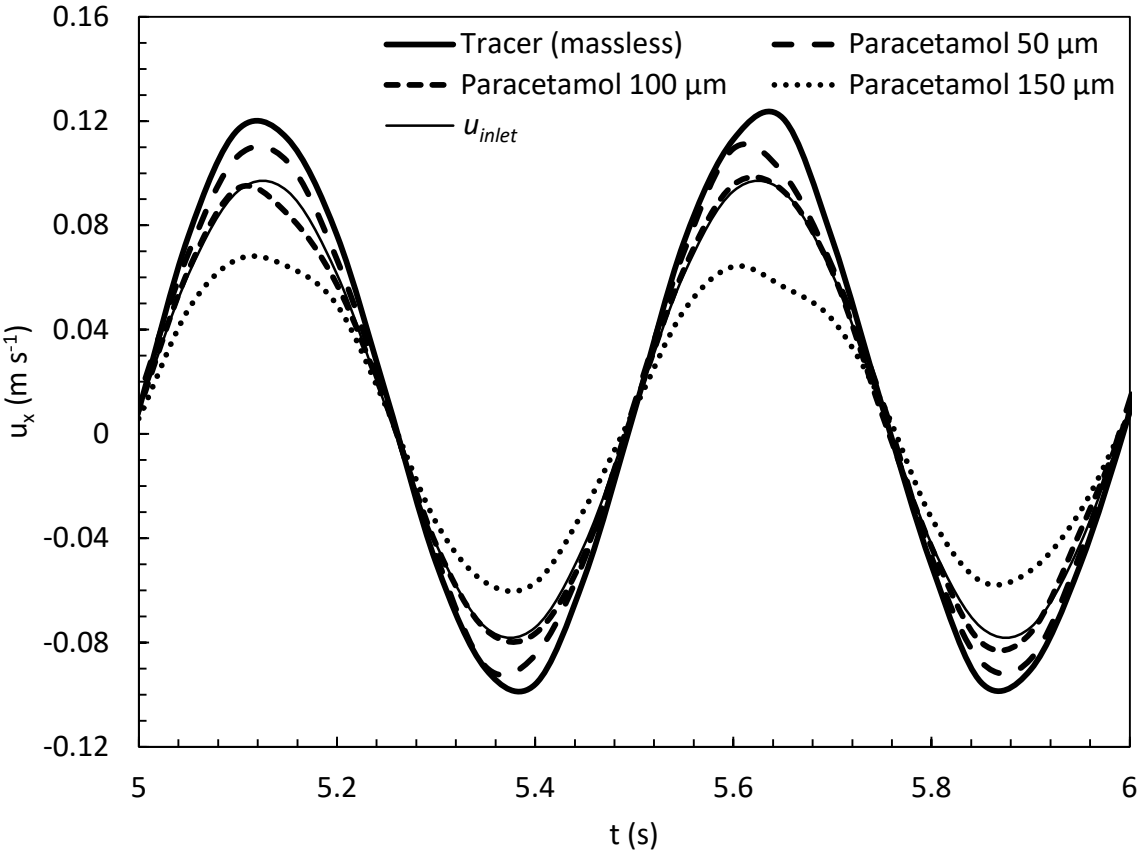

Figure 11. *Axial velocity of particles of different sizes for a certain time range (Q = 100ml/min, f = 2Hz, x_o = 7mm)*

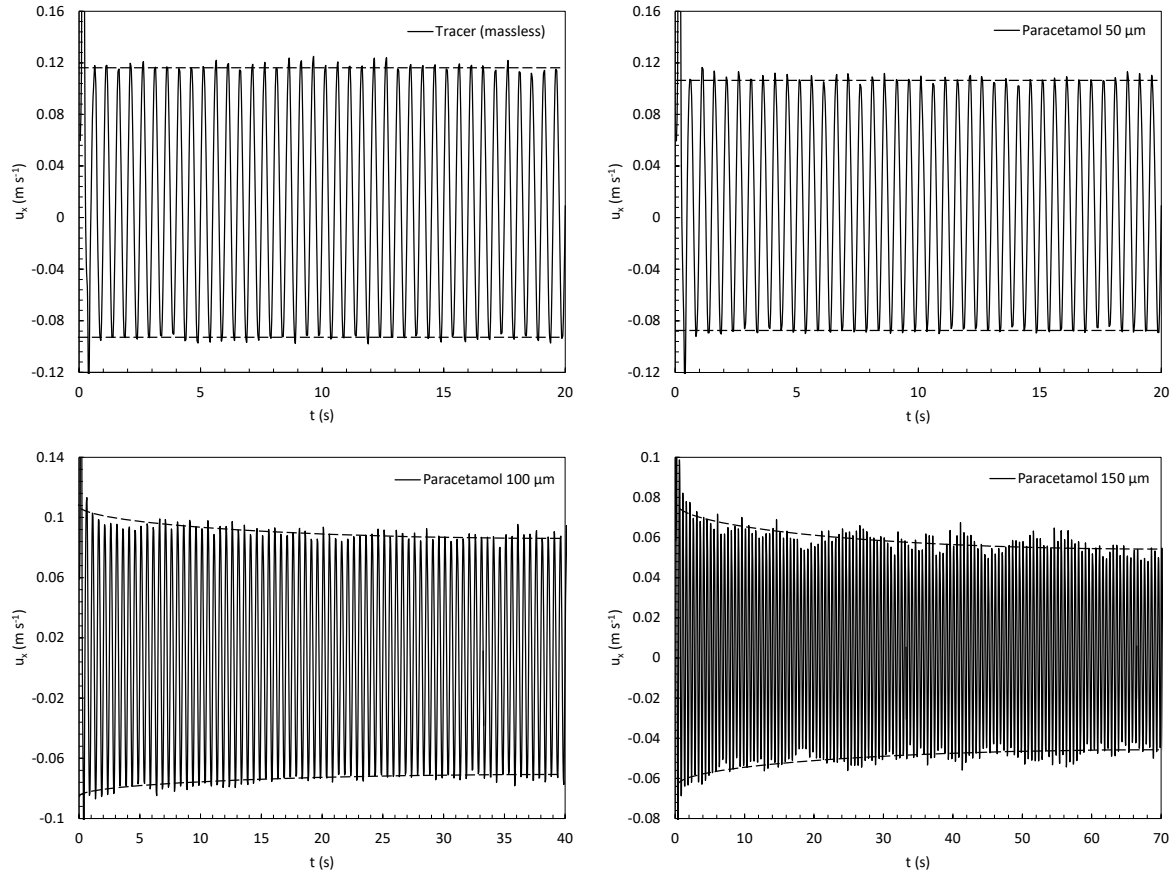

Figure 12. *Axial velocity evolution with time for particles of different sizes (Q = 100ml/min, f = 2Hz, x_o = 7mm)*

The dampening effect of oscillatory velocity, occurring as either particles grow in size or particles of a certain size (100 and 150) move along the reactor, should not be confused with an overall decay in the net axial velocity. While particles of different sizes may experience different oscillatory velocity peaks, their net axial velocities could be identical. Similarly, certain particles may experience a decrease in oscillatory axial velocity, yet maintain a net axial velocity. For this reason, the evolution of the net axial velocity with time should also be analysed. Displaying the evolution of u_x with time for different particle sizes in the same figure can be complex, as the oscillatory velocity peaks from different profiles overlap, preventing the ability to distinguish one from another. To avoid this, the axial velocities and velocity magnitudes obtained from eq. (20) were averaged for each oscillatory cycle and plotted in Figure 13. We see that the liquid phase and small solid particles (50 µm) experience a rather constant trend of net velocity in the axial direction with time, the former fluctuating around the expected u_{net}. On the contrary, paracetamol solids of 100 and 150 µm

diameter have an overall lower net axial velocity, which moderately decays with time. The kinetic energy losses experienced by particles of 100 and 150 µm as they move downstream, whether it is by the dampening of oscillatory velocity or by the reduction of net axial velocity, have a visible impact on the overall velocity magnitude that particles are subjected to, see Figure 13 (right). These findings highlight a potential need of adjusting oscillation conditions, e.g. increasing oscillation amplitude in order to prevent solids settling, depending on the size and terminal velocities of the solids involved.

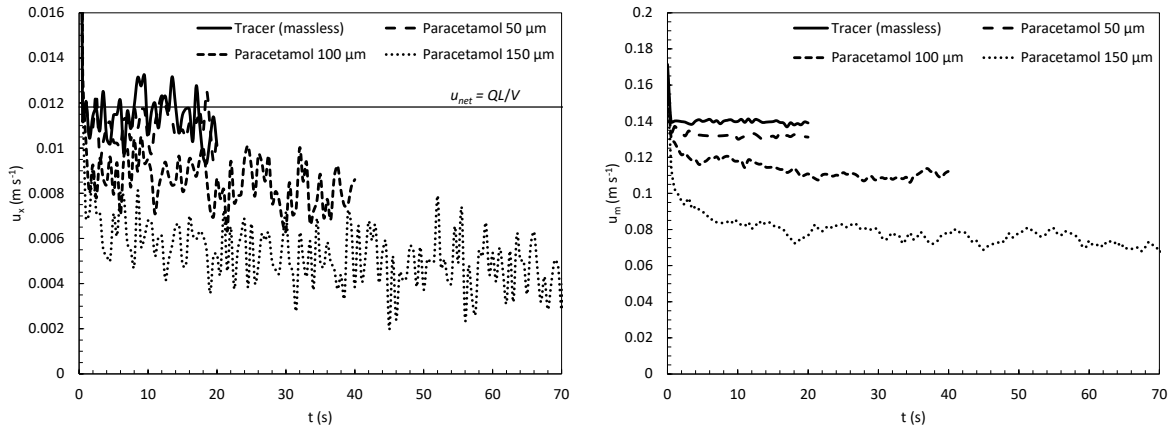

Figure 13. *Average (per cycle) axial velocity (left) and velocity magnitude (right) evolution with time for particles of different sizes (Q = 100ml/min, f = 2Hz, x_o = 7mm)*

The minimum transport velocity required for the suspension of slurry in a horizontal tube (u_{min-h}) is given by the modified Durand equation[61,62]:

$$u_{min-h} = C_{mh}\left[2g\left(\frac{\rho_p}{\rho}-1\right)D\right]\left(\frac{d_p}{D}\right)^{1/6} \tag{21}$$

where D is the diameter of the tube, d_p the diameter of the particle and C_{mh} an empirical constant that ranges from 0.4 to 1.5; taking a conservative approach, a C_{mh} of 1.5 was used in our calculations. Table 4 shows the u_{min-h} required by each set of simulated solid particles, along with the percentage of the time that the oscillatory inlet velocity is higher than the minimum transport velocity, i.e. $\left|u_{inlet}(t)\right| > u_{min-h}$.

Table 4. *Minimum transport velocity (Q = 100ml min^{-1}, f = 2Hz, x_o = 7mm)*

	$u_{min\text{-}h}$ (m s^{-1})	$\left\|u_{inlet}(t)\right\| > u_{min-h}$ (%)
Paracetamol 50 µm	0.0453	65.3
Paracetamol 100 µm	0.0508	60.4
Paracetamol 150 µm	0.0544	57.1

The minimum transport velocity required for slurry suspension in a horizontal tube increases by 20% as particles grow from 50 µm to 150 µm of diameter. The inlet oscillatory velocity is greater in magnitude than $u_{min\text{-}h}$ more than 50% of time for all simulated particles; hence, it is expected for all particles to stay suspended throughout their journey downstream the reactor. However, results point to a decrement in the degree of suspension as particles grow in size.

Suspension of particles was assessed by monitoring their positions in the y-axis throughout all simulated time-steps and averaging it over the total number of particles in the system (N) for each condition as:

$$Position_{y-axis}(t) = \frac{\sum_{i=1}^{N(t)} Position_{y-axis,i}(t)}{N(t)} \tag{22}$$

As expected, Figure 14 shows that the average position in the y-axis decreases as particle size increases. While the suspension for liquid phase and small solid particles (50 µm) occurs at the centre of the device (y = 0), particles of 100 and 150 µm lose height and stay somewhat closer to the bottom wall of the reactor (y = -7.5 mm) as they move axially downstream; these bigger particles are a good example of heterogeneous suspension[61]. Complete settlement of particles was not seen even for the largest particles injected.

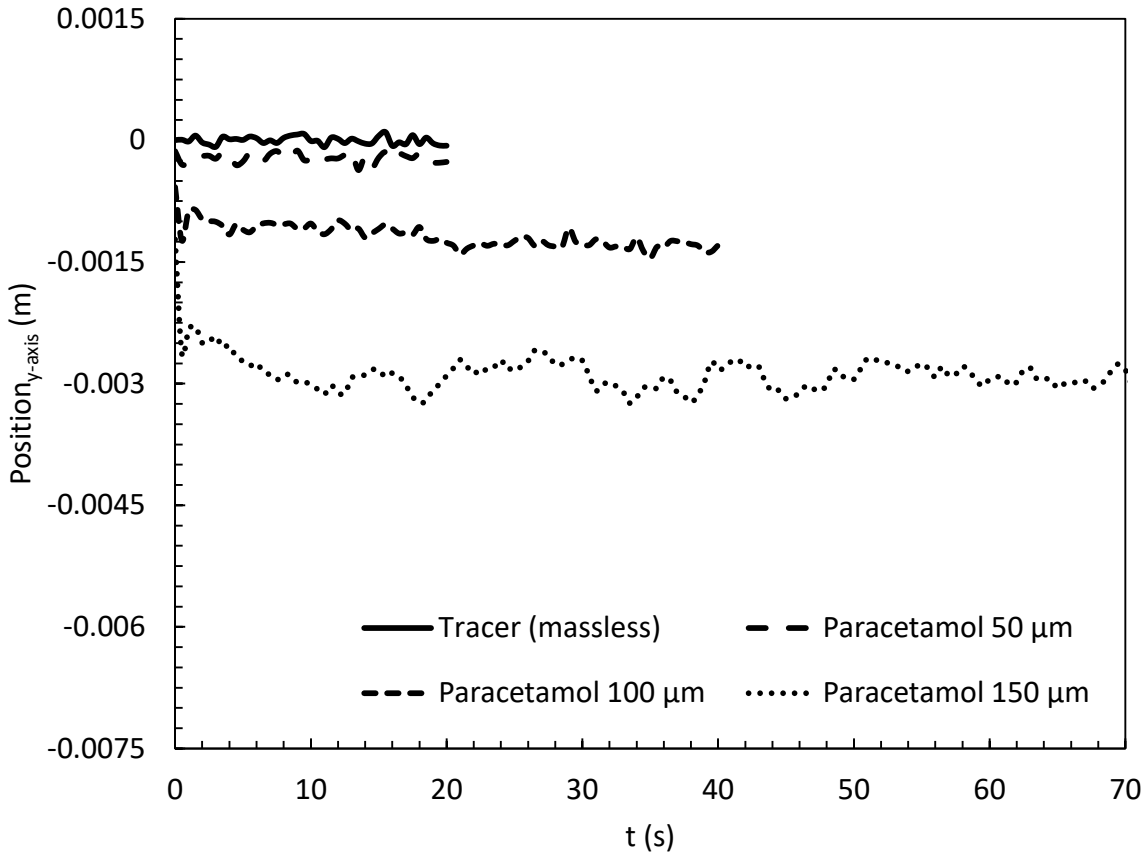

Figure 14. *Position in the y-axis evolution with time for particles of different sizes (Q = 100ml/min, f = 2Hz, x_o = 7mm)*

6. Conclusions

By coupling a primary Eulerian liquid phase with a secondary discrete Lagrangian phase, we have, for the first time, reported a detailed analysis on the effect of particle size on axial dispersion, residence times and velocities experienced by solid particles in a COBR, as well as their impact on solid suspension. Results show a decreasing trend in oscillatory axial velocity as particle size increases, leading to smaller axial dispersion and longer residence times. These findings agree with the work by Ejim et al. and Kacker et al. [30,31].

On the determination of axial dispersion of secondary phase, two methodologies were utilized in this study: the perfect pulse method and the imperfect pulse method. The latter provided constant results at different lengths of the device for all the simulated cases, while the former did not. This is most certainly due to the formulation of the IPM that avoids the assumption of a perfect pulse injection of the secondary phase.

While this work involves mono-size spherical particles simulated at smaller oscillatory amplitudes than those use in crystallization, the understanding of dispersion of a solid phase in liquid is much needed in order to fill the knowledge gap in the area of COBR research and development, where there has been exclusive reliance on correlations obtained from single liquid phase studies.

7. Acknowledgements

The authors wish to thank the EPSRC and Heriot-Watt University for the financial support provided for this project and the Doctoral Training Centre in Continuous Manufacturing and Crystallization EPSRC (EP/K503289/1). We also thank the EPSRC funded ARCHIE-WeSt High Performance Computer (EP/K000586/1).

8. References

1. Mackley MR, Ni X. Mixing and dispersion in a baffled tube for steady laminar and pulsatile flow. *Chemical Engineering Science.* 1991;46(12):3139-3151.

2. Ni X, De Gélicourt YS, Baird MHI, Rao NVR. Scale-up of single phase axial dispersion coefficients in batch and continuous oscillatory baffled tubes. *The Canadian Journal of Chemical Engineering.* 2001;79(3):444-448.

3. Ni X, Zhang Y, Mustafa I. Correction of polymer particle size with droplet size in suspension polymerisation of methylmethacrylate in a batch oscillatory baffled reactor. *Chemical Engineering Science.* 1999;54:841-850.

4. Wilson B, Ni X, Sherrington DC. On the Investigation of a Phase-Transfer Catalysis Reaction in an Oscillatory Baffled Reactor. *Industrial & Engineering Chemistry Research.* 2001;40(23):5300-5304.

5. Phan AN, Harvey AP, Eze V. Rapid Production of Biodiesel in Mesoscale Oscillatory Baffled Reactors. *Chemical Engineering & Technology.* 2012;35(7):1214-1220.

6. Eze VC, Fisher JC, Phan AN, Harvey AP. Intensification of carboxylic acid esterification using a solid catalyst in a mesoscale oscillatory baffled reactor platform. *Chemical Engineering Journal.* 2017;322:205-214.

7. Navarro Fuentes F, Keane MA, Ni X. A comparative evaluation of a multiphase catalytic hydrogenation in an oscillatory baffled reactor

and a stirred tank reactor. *Organic Process Research & Development.* 2018;Submitted.

8. Ni X, Valentine A, Liao A, Sermage SBC, Thomson GB, Roberts KJ. On the Crystal Polymorphic Forms of l-Glutamic Acid Following Temperature Programmed Crystallization in a Batch Oscillatory Baffled Crystallizer. *Crystal Growth & Design.* 2004;4(6):1129-1135.

9. Lawton S, Steele G, Shering P, Zhao L, Laird I, Ni X-W. Continuous Crystallization of Pharmaceuticals Using a Continuous Oscillatory Baffled Crystallizer. *Organic Process Research & Development.* 2009;13(6):1357-1363.

10. Brown CJ, Ni X-W. Evaluation of Growth Kinetics of Antisolvent Crystallization of Paracetamol in an Oscillatory Baffled Crystallizer Utilizing Video Imaging. *Crystal Growth & Design.* 2011;11(9):3994-4000.

11. Brown CJ, Ni X-W. Determination of metastable zone width, mean particle size and detectable number density using video imaging in an oscillatory baffled crystallizer. *CrystEngComm.* 2012;14(8):2944-2949.

12. Callahan CJ, Ni X-W. Probing into Nucleation Mechanisms of Cooling Crystallization of Sodium Chlorate in a Stirred Tank Crystallizer and an Oscillatory Baffled Crystallizer. *Crystal Growth & Design.* 2012;12(5):2525-2532.

13. Brown CJ, Adelakun JA, Ni X-w. Characterization and modelling of antisolvent crystallization of salicylic acid in a continuous oscillatory baffled crystallizer. *Chemical Engineering and Processing: Process Intensification.* 2015;97:180-186.

14. Su Q, Benyahia B, Nagy ZK, Rielly CD. Mathematical Modeling, Design, and Optimization of a Multisegment Multiaddition Plug-Flow Crystallizer for Antisolvent Crystallizations. *Organic Process Research & Development.* 2015;19(12):1859-1870.

15. Agnew LR, McGlone T, Wheatcroft HP, Robertson A, Parsons AR, Wilson CC. Continuous Crystallization of Paracetamol (Acetaminophen) Form II: Selective Access to a Metastable Solid Form. *Crystal Growth & Design.* 2017;17(5):2418-2427.

16. Brown CJ, McGlone T, Yerdelen S, et al. Enabling precision manufacturing of active pharmaceutical ingredients: workflow for seeded cooling continuous crystallisations. *Molecular Systems Design & Engineering.* 2018;3(3):518-549.

17. Ni X. Residence time distribution measurements in a pulsed baffled tube bundle. *Journal of Chemical Technology & Biotechnology.* 1994;59(3):213-221.

18. Ni X. A study of fluid dispersion in oscillatory flow through a baffled tube. *Journal of Chemical Technology & Biotechnology.* 1995;64(2):165-174.
19. Dickens AW, Mackley MR, Williams HR. Experimental residence time distribution measurements for unsteady flow in baffled tubes. *Chemical Engineering Science.* 1989;44(7):1471-1479.
20. Mackley MR, Ni X. Experimental fluid dispersion measurements in periodic baffled tube arrays. *Chemical Engineering Science.* 1993;48(18):3293-3305.
21. Reis N, Vicente AA, Teixeira JA, Mackley MR. Residence times and mixing of a novel continuous oscillatory flow screening reactor. *Chemical Engineering Science.* 2004;59(22–23):4967-4974.
22. Ni X, Brogan G, Struthers A, Bennett DC, Wilson SF. A Systematic Study of the Effect of Geometrical Parameters on Mixing Time in Oscillatory Baffled Columns. *Chemical Engineering Research and Design.* 1998;76(5):635-642.
23. Ni X, Stevenson CC. On the effect of gap size between baffle outer diameter and tube inner diameter on the mixing characteristics in an oscillatory-baffled column. *Journal of Chemical Technology & Biotechnology.* 1999;74(6):587-593.
24. Ni X, Pereira NE. Parameters affecting fluid dispersion in a continuous oscillatory baffled tube. *AIChE Journal.* 2000;46(1):37-45.
25. Ni X, Gélicourt YSd, Neil J, Howes T. On the effect of tracer density on axial dispersion in a batch oscillatory baffled column. *Chemical Engineering Journal.* 2002;85(1):17-25.
26. Zheng M, Mackley M. The axial dispersion performance of an oscillatory flow meso-reactor with relevance to continuous flow operation. *Chemical Engineering Science.* 2008;63(7):1788-1799.
27. Phan AN, Harvey A. Development and evaluation of novel designs of continuous mesoscale oscillatory baffled reactors. *Chemical Engineering Journal.* 2010;159(1–3):212-219.
28. Phan AN, Harvey A, Lavender J. Characterisation of fluid mixing in novel designs of mesoscale oscillatory baffled reactors operating at low flow rates (0.3–0.6 ml/min). *Chemical Engineering and Processing: Process Intensification.* 2011;50(3):254-263.
29. Phan AN, Harvey AP. Effect of geometrical parameters on fluid mixing in novel mesoscale oscillatory helical baffled designs. *Chemical Engineering Journal.* 2011;169(1–3):339-347.
30. Ejim LN, Yerdelen S, McGlone T, et al. A factorial approach to understanding the effect of inner geometry of baffled meso-scale tubes on solids suspension and axial dispersion in continuous,

oscillatory liquid–solid plug flows. *Chemical Engineering Journal.* 2017;308:669-682.

31. Kacker R, Regensburg SI, Kramer HJM. Residence time distribution of dispersed liquid and solid phase in a continuous oscillatory flow baffled crystallizer. *Chemical Engineering Journal.* 2017;317(Supplement C):413-423.

32. Baptista PN, Oliveira FAR, Sannervik J, Oliveira JC. The effect of mixing particles with different characteristics on the residence time distribution of particles in two-phase flow in a tubular system. *Journal of Food Engineering.* 1996;29(3):361-373.

33. Howes T, Mackley MR, Roberts EPL. The simulation of chaotic mixing and dispersion for periodic flows in baffled channels. *Chemical Engineering Science.* 1991;46(7):1669-1677.

34. Jian H, Ni X-W. On modelling turbulent flow in an oscillatory baffled column – RANS model or large-eddy simulation? *Journal of Chemical Technology & Biotechnology.* 2003;78(2-3):321-325.

35. González-Juárez D, Herrero-Martín R, Solano JP. Enhanced heat transfer and power dissipation in oscillatory-flow tubes with circular-orifice baffles: a numerical study. *Applied Thermal Engineering.* 2018;141:494-502.

36. Manninen M, Gorshkova E, Immonen K, Ni X-W. Evaluation of axial dispersion and mixing performance in oscillatory baffled reactors using CFD. *Journal of Chemical Technology & Biotechnology.* 2013;88(4):553-562.

37. Reis N, Vicente AA, Teixeira JA. Liquid backmixing in oscillatory flow through a periodically constricted meso-tube. *Chemical Engineering and Processing: Process Intensification.* 2010;49(7):793-803.

38. Kimuli EN, Onyemelukwe II, Benyahia B, Rielly CD. Characterisation of axial dispersion in a Meso-scale Oscillatory Baffled Crystalliser using a Numerical Approach. In: Espuña A, Graells M, Puigjaner L, eds. *Computer Aided Chemical Engineering.* Vol 40: Elsevier; 2017:223-228.

39. González-Juárez D, Solano JP, Herrero-Martín R, Harvey AP. Residence time distribution in multiorifice baffled tubes: A numerical study. *Chemical Engineering Research and Design.* 2017;118:259-269.

40. Mazubert A, Fletcher DF, Poux M, Aubin J. Hydrodynamics and mixing in continuous oscillatory flow reactors—Part II: Characterisation methods. *Chemical Engineering and Processing: Process Intensification.* 2016;102:102-116.

41. Palma M, Giudici R. Analysis of axial dispersion in an oscillatory-flow continuous reactor. *Chemical Engineering Journal.* 2003;94(3):189-198.

42. Oliva JA, Pal K, Barton A, Firth P, Nagy ZK. Experimental investigation of the effect of scale-up on mixing efficiency in oscillatory flow baffled reactors (OFBR) using principal component based image analysis as a novel noninvasive residence time distribution measurement approach. *Chemical Engineering Journal.* 2018;351:498-505.
43. Vilar G, Williams RA, Wang M, Tweedie RJ. On line analysis of structure of dispersions in an oscillatory baffled reactor using electrical impedance tomography. *Chemical Engineering Journal.* 2008;141(1–3):58-66.
44. Zhao L, Raval V, Briggs NEB, et al. From discovery to scale-up: α-lipoic acid : nicotinamide co-crystals in a continuous oscillatory baffled crystalliser. *CrystEngComm.* 2014;16(26):5769-5780.
45. Briggs NEB, Schacht U, Raval V, McGlone T, Sefcik J, Florence AJ. Seeded Crystallization of β-l-Glutamic Acid in a Continuous Oscillatory Baffled Crystallizer. *Organic Process Research & Development.* 2015;19(12):1903-1911.
46. Levenspiel O, Smith WK. Notes on the diffusion-type model for the longitudinal mixing of fluids in flow. *Chemical Engineering Science.* 1957;6:227-233.
47. Aris R. Notes on the diffusion-type model for longitudinal mixing in flow. *Chemical Engineering Science.* 1959;9(4):266-267.
48. Göebel JC, Booij K, Fortuin JMH. Axial dispersion in single-phase flow in pulsed packed columns. *Chemical Engineering Science.* 1986;41(12):3197-3203.
49. Westerterp KR, Van Swaaij WPM, Beenackers AACM. *Chemical Reactor Design and Operation*: John Wiley & Sons; 1984.
50. Smith KB. *PhD thesis: Scale-up of oscillatory flow mixing*. Cambridge, England: Department of Chemical Engineering, University of Cambridge; 2000.
51. Smith KB, Mackley MR. An Experimental Investigation into the Scale-up of Oscillatory Flow Mixing in Baffled Tubes. *Chemical Engineering Research and Design.* 2006;84(11):1001-1011.
52. Ni X, Jian H, Fitch AW. Computational fluid dynamic modelling of flow patterns in an oscillatory baffled column. *Chemical Engineering Science.* 2002;57(14):2849-2862.
53. Fitch AW, Jian H, Ni X. An investigation of the effect of viscosity on mixing in an oscillatory baffled column using digital particle image velocimetry and computational fluid dynamics simulation. *Chemical Engineering Journal.* 2005;112(1–3):197-210.
54. Reis N, Harvey AP, Mackley MR, Vicente AA, Teixeira JA. Fluid mechanics and design aspects of a novel oscillatory flow screening

mesoreactor. *Chemical Engineering Research and Design.* 2005;83(4):357-371.

55. Mazubert A, Fletcher DF, Poux M, Aubin J. Hydrodynamics and mixing in continuous oscillatory flow reactors—Part I: Effect of baffle geometry. *Chemical Engineering and Processing: Process Intensification.* 2016;108:78-92.

56. Jimeno G, Lee YC, Ni X-W. On the evaluation of power density models for oscillatory baffled reactors using CFD. *Chemical Engineering and Processing - Process Intensification.* 2018.

57. Jian H, Ni X. A numerical study on the scale-up behaviour in oscillatory baffled columns. *Chemical Engineering Research and Design.* 2005;83(10):1163-1170.

58. Ekambara K, Dhotre MT. Simulation of oscillatory baffled column: CFD and population balance. *Chemical Engineering Science.* 2007;62(24):7205-7213.

59. Hamzah AA, Hasan N, Takriff MS, et al. Effect of oscillation amplitude on velocity distributions in an oscillatory baffled column (OBC). *Chemical Engineering Research and Design.* 2012;90(8):1038-1044.

60. Morsi SA, Alexander AJ. An investigation of particle trajectories in two-phase flow systems. *Journal of Fluid Mechanics.* 1972;55(2):193-208.

61. Heywood NI. Stop your slurries from stirring up trouble. *Chem. Eng. Prog.* 1999;95(9):21-41.

62. Yang X, Acevedo D, Mohammad A, et al. Risk Considerations on Developing a Continuous Crystallization System for Carbamazepine. *Organic Process Research & Development.* 2017;21(7):1021-1033.